JGR Atmospheres

RESEARCH ARTICLE
10.1029/2019JD032146

Analysis of the Thermodynamic Phase Transition of Tracked Convective Clouds Based on Geostationary Satellite Observations

Q. Coopman[1], **C. Hoose**[1], **and M. Stengel**[2]

[1]Institute of Meteorology and Climate Research, Karlsruhe Institute of Technology,Karlsruhe,Germany, [2]Deutscher Wetterdienst (DWD),Offenbach,Germany

Key Points:

- A tracking algorithm has been developed to analyze 796 isolated convective clouds that undergo thermodynamic phase transition
- The temporal evolution of cloud parameters have been synchronized at the glaciation
- The phase transition temperature increases up to 11°C for an increase in cloud droplet size by 9 µm

Correspondence to:
Q. Coopman,
quentin.coopman@kit.edu

Citation:
Coopman, Q., Hoose, C., & Stengel, M. (2020). Analysis of the thermodynamic phase transition of tracked convective clouds based on geostationary satellite observations. *Journal of Geophysical Research: Atmospheres*, *125*, e2019JD032146. https://doi.org/10.1029/2019JD032146

Received 28 NOV 2019
Accepted 17 MAY 2020
Accepted article online 21 MAY 2020

Abstract Clouds are liquid at temperature greater than 0°C and ice at temperature below −38°C. Between these two thresholds, the temperature of the cloud thermodynamic phase transition from liquid to ice is difficult to predict and the theory and numerical models do not agree: Microphysical, dynamical, and meteorological parameters influence the glaciation temperature. We temporally track optical and microphysical properties of 796 clouds over Europe from 2004 to 2015 with the space-based instrument Spinning Enhanced Visible and Infrared Imager on board the geostationary METEOSAT second generation satellites. We define the glaciation temperature as the mean between the cloud top temperature of those consecutive images for which a thermodynamic phase change in at least one pixel is observed for a given cloud object. We find that, on average, isolated convective clouds over Europe freeze at −21.6°C. Furthermore, we analyze the temporal evolution of a set of cloud properties and we retrieve glaciation temperatures binned by meteorological and microphysical regimes: For example, the glaciation temperature increases up to 11°C when cloud droplets are large, in line with previous studies. Moreover, the correlations between the parameters characterizing the glaciation temperature are compared and analyzed and a statistical study based on principal component analysis shows that after the cloud top height, the cloud droplet size is the most important parameter to determine the glaciation temperature.

Plain Language Summary It is difficult to quantify the temperature at which clouds transition from liquid to ice. Indeed, between −38°C and 0°C, clouds can be composed of liquid cloud droplets, ice crystals, or mixture of both, but the theory cannot predict the observations. Satellites usually give a snapshot of microphysical properties of clouds at one time step during their lifetime. Therefore, statistical tools are needed to infer how clouds behave during their life cycle from a composite of several clouds. Here, we temporally track the properties of 796 convective clouds over Europe from a tracking algorithm based on the geostationary satellite SEVIRI. We are able to study the same clouds from their initiation to their dissipation including their transition from liquid to ice with a temporal resolution of 15 min. We find that, on average, clouds freeze at −21.6°C and that the size of cloud droplets has a large impact on the temperature of glaciation: The larger the cloud droplets, the higher the temperature of glaciation. Our results aim to better understand how clouds transition from liquid to ice, and they can improve predictions of the impact of clouds in future climate.

1. Introduction

The cloud thermodynamic phase impacts cloud radiative properties, cloud lifetime, and dynamical properties. Unfortunately, processes that determine the phase transition are still poorly understood and theory, observations, and in situ measurements still disagree, which leads to large uncertainties (Cantrell & Heymsfield, 2005): For example, Komurcu et al. (2014) observed that the ice water path is underestimated by more than 70 g/m^2 in models compared to satellite observations from MODerate resolution Imaging Spectroradiometer (MODIS).

Below −38°C, clouds are in the ice phase and above 0°C, clouds are in the liquid phase. Between −38°C and 0°C, clouds can be either liquid, ice or a mixture of the two phases and different parameters influence the phase transition: For example, aerosols can act as ice nuclei, while large cloud droplets are more prone to secondary ice production (Rosenfeld et al., 2011); both examples potentially increase the glaciation

temperature (T_g). Parameters, such as the cloud droplet size and aerosol concentration, can be correlated or anti-correlated with each other, and it is therefore difficult to disentangle their respective effect on T_g (Coopman et al., 2018; Gryspeerdt et al., 2016).

Detection of cloud phase transition using observations is not trivial. In situ observations provide high-resolution measurements associated with low uncertainties. Unfortunately, studies from field campaigns last only for weeks or months and are spatially constrained. Therefore, it is difficult to obtain long time series. On the opposite, satellite observations offer long time measurements and cover an extended area. But, the uncertainties associated with the measurements are large and the information only comes from cloud tops for passive instruments and from a spatially restricted area of a laser or radar beam for active instruments. Moreover, from polar orbiting satellites, statistical analysis is performed on the probability of glaciation for different regimes but we cannot study the temporal evolution of the phase transition for one cloud.

Cloud properties can be tracked over time with geostationary satellites. Geostationary satellites have been widely used to detect convective initiation (i.e., Mecikalski & Bedka, 2006; Mecikalski et al., 2010a, 2010b; Roberts & Rutledge, 2003, 2010a; Zinner et al., 2008). Other studies have been analyzing the evolution of cloud parameters: For example, Senf et al. (2015) and Senf and Deneke (2017) applied their algorithm to 9 and 151 clouds, respectively, and studied the evolution of microphysical and macrophysical parameters of clouds taking as a reference the maximum cloud top cooling rate. Patou et al. (2018) coupled satellite observations with numerical models, and they followed the evolution of precipitation for 35 cases. Schröder et al. (2009) analyzed the spatial distribution of deep convective clouds over Africa based on brightness temperature changes. Zinner et al. (2008) developed a very comprehensive tool to track convective cells based on geographical overlap. Bley et al. (2016) tracked 30 clouds to study warm convective clouds over Europe. Walker et al. (2012) studies the initiation of convection over the United States with 804 cases. Heikenfeld et al. (2019) developed a flexible method based on the synergy of model simulations and observations and on the maximum vertical velocity, which is promising to track deep convective clouds. In most of the previous studies, the number of tracked clouds is less than 100, which limits the significance of statistical analysis. Moreover, none of the former studies focused on the liquid-to-ice phase transition nor retrieved glaciation temperatures.

Lensky and Rosenfeld (2006) have shown that the tracking of clouds is not necessary because the temporal evolution of cloud properties are exchangeable with the instantaneously properties of a field of clouds that contains cells at various stages of their lifecycle. Nevertheless, Yuan et al. (2010) have pointed out that at least 100 pixels per temperature bin are needed to free results from natural variability and retrieval uncertainty. Therefore, the method is suited for large cloud systems or large ensembles but not for isolated convective clouds.

In the current study, we track convective clouds from a geostationary satellite focusing on the thermodynamic phase transition. We aim to understand which parameters trigger or inhibit the phase transition. The next section presents the data set used from a space-based observation, the tracking algorithm, and the statistical tools. We divide our result section in three main parts: First, we analyze the temporal evolution of cloud properties, then we study the difference in T_g for different meteorological and microphysical regimes, and we present results from a statistical analysis to discuss the correlations that the different parameters have with each others and how they impact T_g.

2. Data And Method

2.1. Satellite Observations

The Spinning Enhanced Visible and Infrared Imager (SEVIRI) sensor on board the geostationnary METEOSAT second generation satellites provides measurements with a temporal resolution of 15 min and a spatial resolution of 3 km at the subsatellite point for 11 spectral channels (12 channels in total). These measurements were used to derive cloud properties composing the CLoud property dAtAset using SEVIRI - edition 2 (Benas et al., 2017; Stengel et al., 2014). Details on the retrieval algorithms are given in Benas et al. (2017). Here, we highlight the features that are most important for the present study.

A series of spectral tests as a function of illumination for different surface types among other factors are performed to detect clouds, resulting in each pixel being classified as either cloud filled, cloud free, cloud

contaminated, or snow/ice contaminated (Derrien & Le Gléau, 2005; Derrien, 2013). In the present study, we only consider cloud filled pixels.

Cloud top pressure (CTP) is retrieved from infrared measurements compared with clear-sky and cloudy radiative transfer simulations using the Radiative Transfer for TOVS (RTTOV Matricardi et al., 2004; Saunders et al., 1999), using ERA-Interim (Dee et al., 2011) as input, applying the H_2O infrared window intercept method (Schmetz et al., 1993) and the radiance rationing method (Menzel et al., 1983). Cloud top temperature (CTT) is retrieved from CTP using ERA-Interim profiles.

The cloud top phase retrieval is based upon a decision tree with several spectral tests involving measurements from 5 spectral channels from 6.2 to 13.4 μm and simulated clear and cloudy sky radiances using RTTOV (Matricardi et al., 2004; Saunders et al., 1999). Clouds are classified into six categories: liquid, supercooled, opaque ice, cirrus, overlap, and overshooting. The six categories are then converted to a binary cloud phase, ice or liquid (Benas et al., 2017). It is important to note that in CLAAS-2, cloud top phase and CTT are retrieved independently from each other with the exceptions that ice pixels are reclassified as liquid if CTT is greater than 0°C and liquid pixels are reclassified as ice if CTT is lower than −38°C.

Effective radius (r_e) and optical thickness (τ) are retrieved following a Nakajima and King (1990) approach based on the channels at 0.6 and 1.6 μm (Meirink & van Zadelhoff, 2016; Roebeling et al., 2006) and the double Adding KNMI radiative transfer model (Stammes, 2001).

Before all retrievals are carried out, the visible and near-infrared measurements were recalibrated following Meirink et al. (2013). For our analysis, we use so-called Level-2 data (pixel data with 15 minute and 3 km × 3 km resolution) in June, July, and August, more favorable to convection, from 2004 to 2015 during daytime, over Europe—with latitudes between 37°N and 56°N and longitudes between 2°W and 24°E.

2.2. Cloud Tracking Algorithm

We analyze the temporal evolution of clouds by employing a cloud tracking algorithm. Most algorithms require manual detection (e.g., Mecikalski et al., 2016; Senf et al., 2015; Senf & Deneke, 2017) and/or are computationally expensive (e.g., Zinner et al., 2008). We developed an algorithm that is automatic and can be run over several years. The algorithm, based on cloud-object overlaps, needs three steps. The first step corresponds to the implementation of the cloud object identification, the second step corresponds to the object overlap between two consecutive time steps, and the last step selects the cases following several criteria. The three steps are described below:

First, we consider cloudy pixels during daytime with an optical thickness greater than 0.3 to avoid retrieval issues associated with thin clouds and surface contamination (Roebeling et al., 2006; Platnick et al., 2014). We define a cloud object: a pixel cluster with eight connected cloudy pixels. As we are interested in isolated convective clouds when they transition from liquid to ice, we exclude cloud object with a size greater than 4,500 pixels corresponding to 112,500 km^2 to avoid large cirrus or anvils which have already been glaciated. Furthermore, the cloud objects need to have a size greater than 40 pixels corresponding to 1,000 km^2 to ensure that the overlap of two cloud masks between two subsequent time steps corresponds to the same cloud (Schröder et al., 2009; Zinner et al., 2008). For each cloudy pixel that fulfills the criteria mentioned above, we start the potential tracking.

In the second step, consecutive measurements are analyzed, which are 15 min apart from each other (Mathon & Laurent, 2001): A cloud can be temporally tracked as long as cloud areas between two consecutive time steps intersect. To avoid splitting or merging cloud object distorting the statistics, we do not consider clouds for which the area variation between two time steps is higher than 50%. If a cloud splits and the two successors do not overlap more than 50% with the former cloud, we disregard this case. If it does, we continue the tracking with the cell that overlaps the most with the former cloud. When there are no cloudy pixels that follow the overlapping criteria, we stop the tracking.

In the final step, we collect the cloud properties of the coldest pixel of a cloud object for each time step, in line with Coopman et al. (2019). The transition of the cloud phase of the coldest pixel from liquid to ice represents the initiation of the thermodynamic phase transition of the tracked cloud. Repeating this procedure but considering the two percent coldest pixels instead (as described by Schröder et al., 2009, and Mecikalski et al., 2016) did not change the results significantly. In the aim to avoid that the coldest pixel jumps from one cloud region to an other between two time steps, we only consider clouds for which the coldest pixel moves

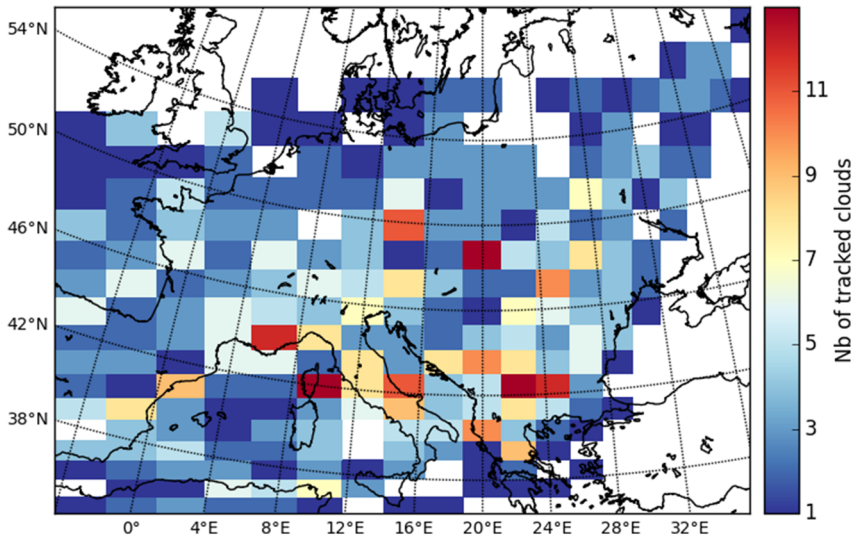

Figure 1. Spatial distribution of the tracked clouds for which we observe a thermodynamic phase transition of the coldest pixel.

less than 20% of the cloud area within 15 min. We only keep clouds for which we observe a phase transition of the coldest pixel. We require that the clouds have at least two time steps in the liquid phase and two time steps in the ice phase. We further exclude clouds for which we observe phase transitions back and forth in the liquid and ice phase, so only clouds which transition only once are considered. We focus our research on the boreal summer, more prone to convection. From 2004 to 2015, between June and August, we are able to track 796 clouds that match all of the named conditions. For each tracked clouds, we retrieve the glaciation temperature (T_g) as the average temperature before and after the phase transition, and we consider the time between the last detected liquid and first detected ice as the reference time t_0.

Figure 1 shows the spatial distribution of the tracked clouds given the criteria mentioned above. A slightly higher number of clouds are tracked in the surrounding of the Adriatic Sea compared to the other regions, but otherwise they are homogeneously distributed over the investigated domain emphasizing that the results presented here are not characteristic to a specific region within Europe.

2.3. ERA-Interim

ERA-Interim (ERA-I) reanalysis data from ECMWF (Berrisford et al., 2011) extend from 1989 to the present. ERA-I has been improved for the representation of the hydrological cycle, the quality of the stratospheric circulation, and the consistency in time of the reanalyzed fields in 2011 (Dee et al., 2011). The temporal resolution is 6 hr with sixty pressure levels and a spatial resolution of 0.75° × 0.75°. Dee et al. (2011) provided a full description of ERA-I parameters and the performance of the algorithms. We use the the most unstable convective available potential energy (CAPE) and the vertical pressure velocity at 500 hPa (ω_{500}) calculated by ERA-Interim. CAPE is retrieved between the level of free convection (LFC) and the level of neutral buoyancy (LNB) as

$$\mathrm{CAPE} = \int_{LFC}^{LNB} R_d(T_{vp} - T_{ve}) d\ln P, \tag{1}$$

where R_d, T_{vp}, T_{ve}, and P are, respectively, the gas constant for dry air, the virtual temperature of the air parcel, the virtual temperature of the environment, and the pressure. Due to the temporal resolution, the CAPE considered in the study might already be depleted by the convection. Unfortunately, it is not possible to have CAPE before the convection.

2.4. Principal Component Analysis

The principal component analysis (PCA) is used to reduce a large number of parameters into a fewer number of components to describe the variability of a data set. It uses a linear combination of a set of variables.

Data and their variability are described in a space of n dimensions. The PCA aims to transform the base of n parameters to a base of m components. The maximum number of components is n, but the variability

of the data can potentially be described with m lower than n. Therefore, the parameters are described as a linear combination of the components that are orthogonal to, or independent of each other. There are several methods to determine the final number of components $m$needed to describe the variability of the data (Velicer, 1976). We use the Kaiser criterion, which is used for the factor analysis, but it can be applied to the PCA: Components with eigenvalues of the covariance matrix less than one are discarded; that is, we only keep the components for which the eigenvalue is greater than the information considering an average of single item (Costello & Osborne, 2005). From the PCA, we can rank the importance of the $n$parameters to describe the variability of the data but also to describe the correlation between the parameters. The different parameters are normalized to range from zero to one to ensure that their impacts on the variability of the data is not overestimated or underestimated due to their range.

Here, we are interested in the impact of the parameters on T_g, so we define different regimes based on the temperature. We define 20 intervals of T_g with thresholds at every fifth percentile such that each T_g regime has approximately 40 tracked clouds. For each regime, we average the microphysical and dynamical properties. It should be noted that the results presented here are not sensitive to the number of T_g regimes: We did the same analysis changing the number of clouds per bin from 30 to 50 and the conclusions did not change (not shown here).

Regarding our data set, we need to define the n dimensions to describe the variability of T_g from the cloud and atmospheric properties. The different parameters are described in sections 2.1 and 2.3, but for each tracked cloud, we need to define a time step for which the parameters are considered. We consider the cloud droplet size two time steps before the phase transition because of artifact effects around the phase transition (Coopman et al., 2019) to study the droplet size impact on T_g. Similar to the cloud droplet size, we consider the size of ice crystal after the phase transition. We want to observe the altitude where the cloud transition from ice to liquid, so we consider CTH at the phase transition. ERA-Interim output has a temporal resolution of 6 hr, so we consider the closest value of the phase transition for CAPE and ω_{500}. Anvil area is an important parameter to determine the net radiative effect of clouds; therefore, we consider the maximum size the tracked clouds have during their life time. Then, each tracked cloud can be defined by six parameters: the maximum cloud area (A^{max}), the cloud top height at the phase transition ($CTH(t_0)$), r_e^{Liq} two time steps (Δt) before the phase transition ($r_e^{Liq}(t_0 - 2\Delta\ t)$), r_e^{Ice} two Δt after the phase transition ($r_e^{Ice}(t_0 + 2\Delta\ t)$), CAPE, and ω_{500} both considered at the closest time to t_0 ($CAPE(t_0)$ and $\omega_{500}(t_0)$).

We define the Matrix A of dimension 20×6 as

$$A = \begin{pmatrix} \overline{A_1^{max}} & \overline{r_{e,1}^{Liq}(t_0 - 2\Delta t)} & \overline{r_{e,1}^{Ice}(t_0 + 2\Delta t)} & \overline{CTH_1(t_0)} & \overline{CAPE_1(t_0)} & \overline{\omega_{500,1}(t_0)} \\ \overline{A_2^{max}} & \overline{r_{e,2}^{Liq}(t_0 - 2\Delta t)} & \overline{r_{e,2}^{Ice}(t_0 + 2\Delta t)} & \overline{CTH_2(t_0)} & \overline{CAPE_2(t_0)} & \overline{\omega_{500,2}(t_0)} \\ \vdots & \vdots & \vdots & \vdots & \vdots & \vdots \\ \overline{A_{20}^{max}} & \overline{r_{e,20}^{Liq}(t_0 - 2\Delta t)} & \overline{r_{e,20}^{Ice}(t_0 + 2\Delta t)} & \overline{CTH_{20}(t_0)} & \overline{CAPE_{20}(t_0)} & \overline{\omega_{500,20(t_0)}} \end{pmatrix}, \quad (2)$$

where the subscripts $(1, 2, \ldots, 20)$ represent the different T_g regimes that correspond to the sampling of the analysis and the over bar indicates that we consider the mean over each temperature range.

In the aim to find a new orthogonal base, the eigenvectors and eigenvalues are retrieved from the covariance matrix of A:

$$\alpha_i \vec{F_i} = cov(A)\vec{F_i}, \quad (3)$$

where α_i is the eigenvalue and $\vec{F_i}$ the eigenvector with i ranging from 1 to 6. The dimension of $\vec{F}$ and cov(A) are, respectively, 6 and 6×6.

The eigenvectors define the components, and they are independent from each other. Each component is described by a linear combination of the parameters:

$$\vec{F_i} = (\beta_{i,1}, \beta_{i,2}, \ldots, \beta_{i,6})^T(\overrightarrow{A^{max}}, \overrightarrow{CTH(t_0)}, \ldots, \overrightarrow{\omega_{500}(t_0)}), \quad (4)$$

where $\beta_{i,j}$ are the indexes of $\vec{F_i}$ in the base $(\overrightarrow{A^{max}}, \overrightarrow{CTH(t_0)}, \ldots, \overrightarrow{\omega_{500}(t_0)})$.

The PCA enables the ranking of components for describing the variability of T_g through the eigenvalues, and subsequently, it is possible to qualitatively rank the importance of the initial parameters to describe the variability. Moreover, in the orthogonal space defined by the components, the collinearity of the parameters informs on the intercorrelation between the parameters themselves.

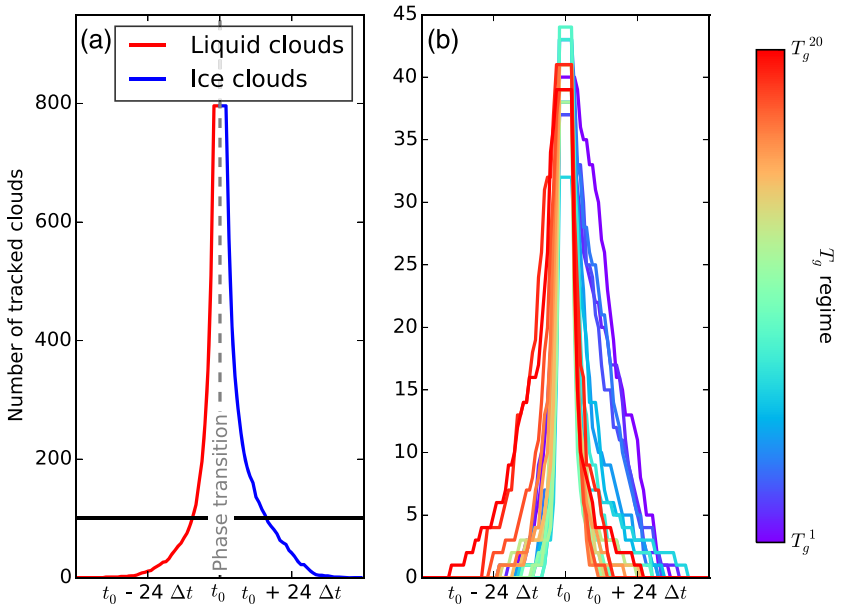

Figure 2. (a) Number of tracked clouds for each time step before and after the reference time (t_0) defined by the phase transition. The horizontal black line represents the thresholds we use in section 3.1. (b) Same as (a) but for the 40 regimes binned by T_g.

3. Results

We divide the result section in three distinct parts. The first part describes the temporal evolution of cloud microphysical properties. The second part provides an analysis of T_g for different meteorological or microphysical regimes. Finally, the last part presents the analysis of the variation of T_g and the covariability between the different parameters.

3.1. Temporal Evolution

We analyze the mean temporal evolution of the different parameters by building a composite from the 796 tracked clouds with the reference time t_0. Figure 2a shows the temporal evolution of the number of clouds that we are able to track for each time step. The four time steps around the phase transition have the same number of data point because each tracked cloud is required to have at least two time steps in the liquid phase and two time steps in the ice phase. The further from the phase transition, the smaller the number of tracked clouds. We only consider time steps for which we have at least 100 tracked clouds in the aim to retrieve statistically significant averages.

Figure 3a shows the CTT of the coldest pixels averaged over the tracked clouds associated with the standard deviation. The temperature is relatively constant over the liquid phase and then decreases slightly before the phase transition: The mean CTT decreases from +1.0°C to −13.6°C over the liquid phase. At the phase transition, the mean CTT goes from −13.6°C to −31.1°C, decreasing by 17.5°C, and further decreases to −53.9°C at time $t_0 + 14, \Delta t$, and remains below −50°C afterwards. The standard deviation never exceeds 4.2°C. We observe that the maximum of cloud-top cooling happens at the phase transition.

Similarly, we retrieve the mean temporal evolution of different parameters. Figure 3b shows the mean temporal evolution of CTH. CTH and CTT are directly related with each other in CLAAS-2 (Benas et al., 2017). As described in Figure 3a, we observe that CTH increases in the liquid phase, then it is accelerated at the phase transition and finally reach a plateau around 10 km corresponding to the midlatitude tropopause.

We have CTH at different time steps apart 15 min, so we can derive the apparent ascent speed of the cloud top of a cluster of convective towers seen at the satellite sensor resolution between two time steps as

$$w = \frac{\Delta\ CTH}{\Delta\ t}, \tag{5}$$

with w the apparent ascent speed of the cloud top. Figure 3c shows the mean cloud-top apparent ascent speed retrieved from Figure 3b and Equation 5. We observe that the mean apparent ascent speed of the cloud

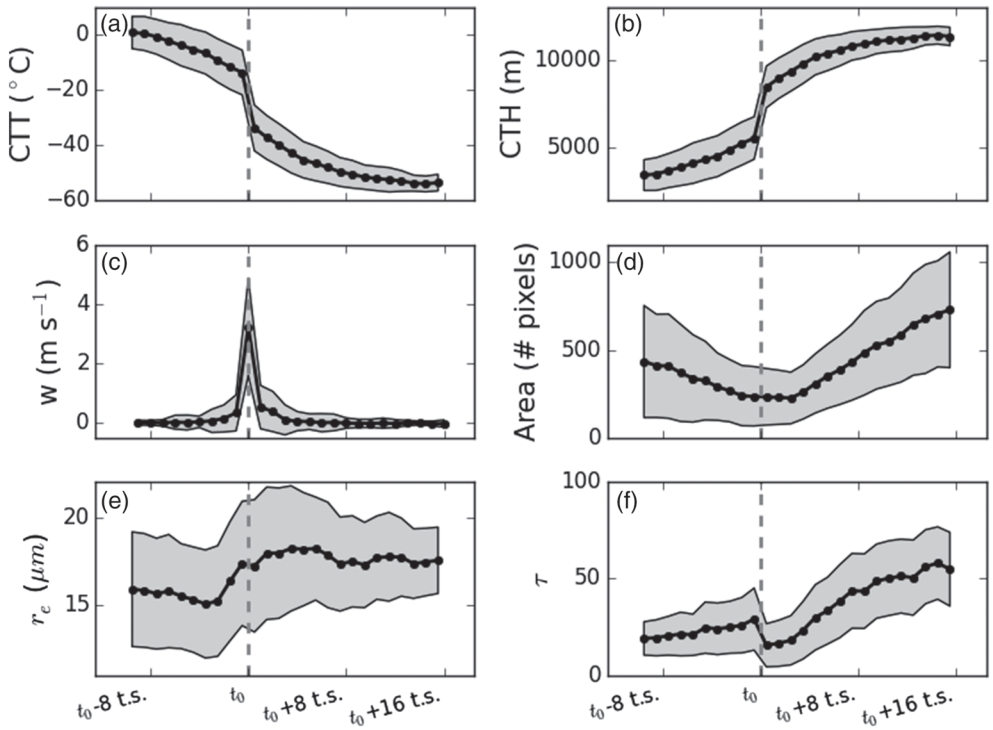

Figure 3. (a) Average of the temporal evolution of the cloud top temperature for 796 tracked using the phase transition time as a reference and the shaded area represents the standard deviation. The sub-figure *b* is the same as *a* but for the cloud top height (CTH), *c* for the apparent ascent speed of the cloud top (w), *d* for the cloud area, *e* for cloud particle radii (r_e), and *f* for the median of cloud optical depth (τ).

top is small but positive for every time step in the liquid phase: w is less than 0.3 m/s. w reaches a peak at the phase transition of 3.2 m/s and then decreases in the ice phase. Senf and Deneke (2017) also retrieved a maximum cloud-top ascent of 3 m/s for isolated convective clouds over Europe using the SEVIRI temporal resolution of 5 min. In their study, they were able to detect that the freezing prompts a maximum cloud top cooling rate possibly due to a release of latent heating which lead to a maximum in w.

Figure 3d shows the mean temporal evolution of the cloud area. In the liquid phase, we observe a decrease in the cloud area from 10,887 to 5,695 km^2. In the ice phase, the cloud area increases from 6,550 km^2 to 18,220 km^2. The increase in the ice phase can be explained by the development of the cloud during the convective phase, which grows in size as it is expected for convective clouds when they vertically develop and reach the tropopause.

On the opposite, the decrease in the liquid phase is not expected, and it is an artifact produced by the tracking algorithm. Indeed, the algorithm is based on the overlap between two successive images; it is therefore easier to track large clouds than small clouds for a longer time: As we approach the phase transition, small clouds are included in the average, decreasing the mean of the area. For example, for tracked clouds with a life time in the liquid phase greater than eight time steps, the area increases on average by 69 pixels between the first measurements in the liquid phase and before the phase transition. The cloud area for long lived clouds in the liquid phase increases over time, which is contrary to the results shown in Figure 3d. If we do the same analysis for tracked clouds with a life time in the ice phase greater than eight time steps, the area increases on average by 50 pixels between the first and the last measurements in the ice phase. We observe an increase of the cloud area in the ice phase with time, as described in Figure 3d.

Figures 3e and 3f show the temporal evolution of the effective radius and the optical thickness of the convective clouds, respectively. Regarding r_e, we observe an increase in the liquid phase: r_e goes from 15.9 μm at $t_0 - 12\Delta t$ to 17.4 μm at $t_0 - 1\Delta t$, then reaches a plateau at the phase transition, then r_e^{Ice} increases for 1 hr and then decreases to reach a plateau around $r_e^{Ice} = 17.5$ μm. The increase of r_e is characteristic of convective clouds in the liquid phase: The updraft transports the water vapor allowing the cloud droplets to grow. The decrease in the ice phase can indicate a mature state: The ice crystal size of the anvil is usually smaller

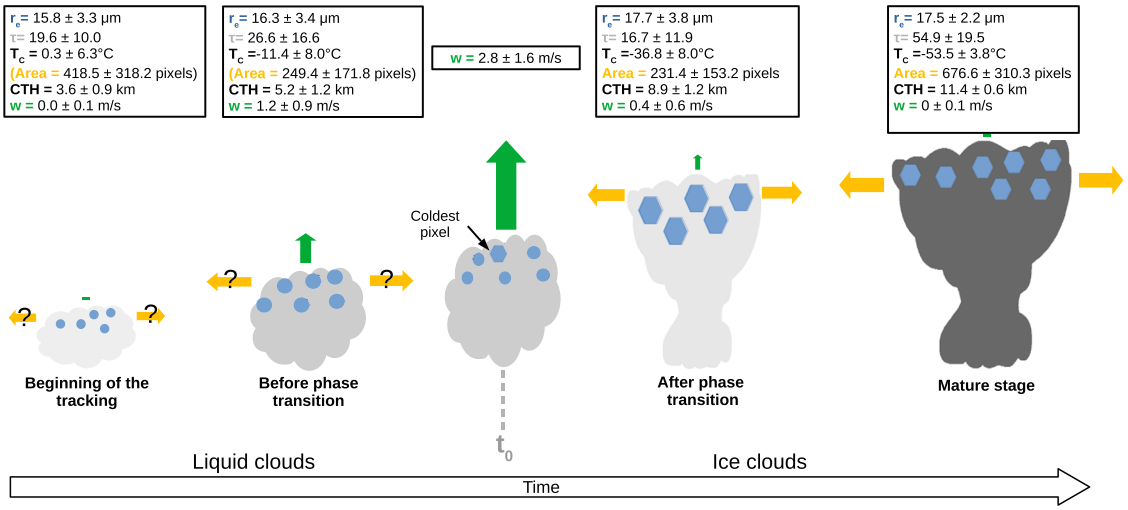

Figure 4. Summary of the temporal evolution of clouds for the different time steps from the initiation to maturation based on 796 tracked clouds. The numbers in the rectangles correspond to the averaged first three time steps for the beginning of the tracking, three time steps before the phase transition, three time steps after the phase transition, and the last three points for the maturation from Figure 3 and the standard deviation.

than at the core due to the sedimentation of large ice crystals and the sublimation of ice when the cloud dissipates (Jensen et al., 2009).

For τ, we did not consider the arithmetic mean because 10% of the tracked clouds have τ greater than 100 during their lifetime, which is the limit for the retrieval. Therefore, the mean would not be representative of the evolution, Figure 3f shows the median evolution of τ and the gray area is the lower and upper quartiles. We observe that the median of τ is constant around 22.1 in the liquid phase and decreases to 15.1 at the phase transition. The decrease of τ at the phase transition can be explained as ice crystals are larger but fewer than cloud droplets. After the phase transition, we observe that the median τ increases up to 58.1 at the mature stage.

In Figures 3e and 3f, we observe a decrease of r_e at the phase transition as already described by Coopman et al. (2019): The reason for this apparently unphysical feature is that the values of r_e depend on the thermodynamic phase retrieved by the algorithm beforehand. Unfortunately, CLAAS-2 does not consider mixed-phase clouds that lead to a bias in cloud microphysical property retrievals. The r_e^{Liq} is artificially increased if the pixel is mixed phase because the ice is more absorbing in the near infrared than the liquid and it biases measurements in the Nakajima and King (1990) retrievals. On the opposite, r_e^{Ice} is artificially decreased if the pixel is mixed phase.

In Figure 4, we propose a schematic view of the evolution of cloud properties along different time steps: at the beginning of the tracking, before, at, and after the phase transition, and at the mature stage. At the beginning of the tracking, clouds have on average small cloud droplets, τ and CTH are low and the CTH increases slowly. Before the phase transition, cloud droplets grow, the apparent ascent speed of the cloud top increases slightly, and the optical depth is almost constant. At the phase transition, the updraft reaches its maximum. After the phase transition, the ice crystal size, the cloud area, and τ increase and CTH increases but at a slower pace than at the phase transition. In the last stage, the cloud area, optical thickness, and CTH increases and the ice crystal size decreases.

3.2. Variation of Glaciation Temperature

T_g is defined as the mean between the last coldest liquid-pixel and the first-ice pixel temperatures, so T_g can be lower than −38°C if the last coldest liquid pixel is slightly higher than −38°C and the first coldest ice pixel is significantly lower than −38°C for example. Similarly, T_g can be greater than 0°C if the last coldest liquid pixel is significantly higher than 0°C and the first coldest ice pixel is slightly lower than 0°C for example. Considering the time resolution of 15 min, T_g for one tracked cloud does not necessarily represent the phase transition. Indeed, the phase transition may have happened at a temperature close to the temperature of the last liquid pixel or first ice pixel. Nevertheless, if we consider the median of several cases, we can retrieve a statistical value of T_g. For the 796 clouds, we retrieve $T_g = -21.6$°C (−33.6; −12.5), with the

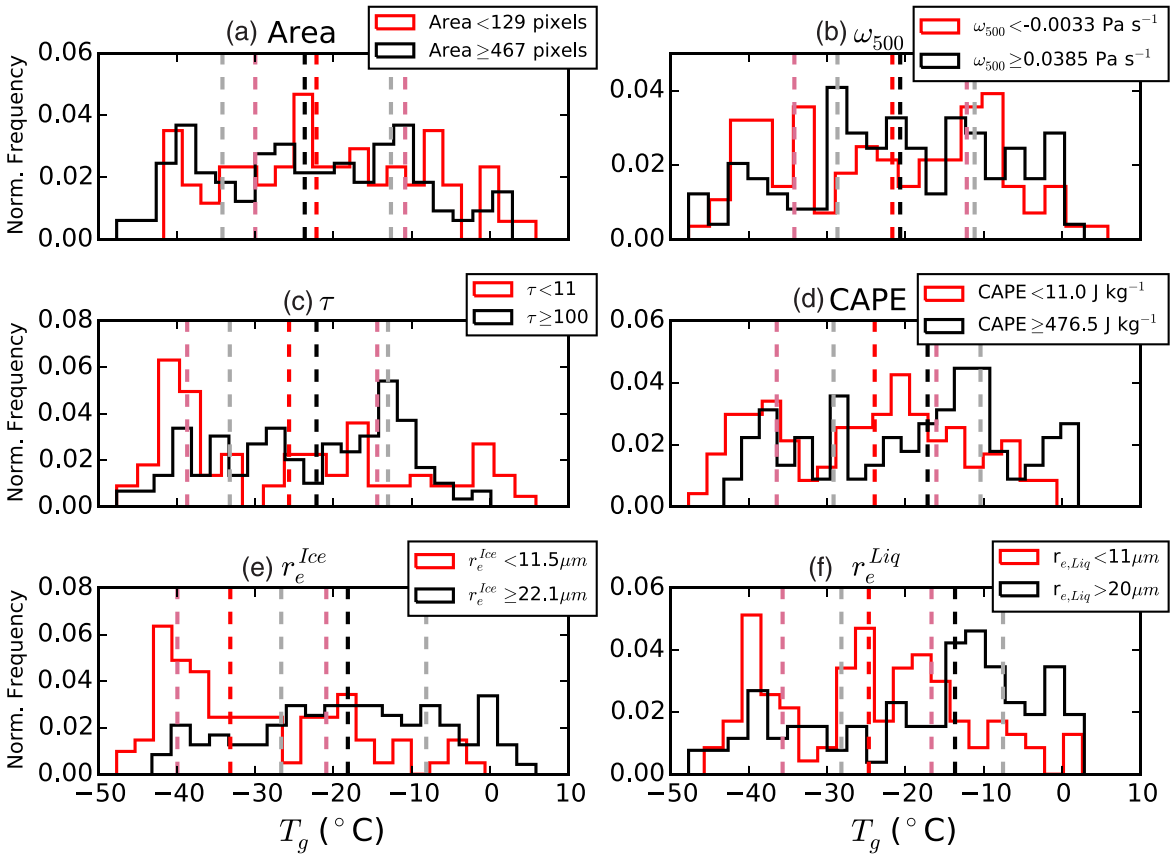

Figure 5. (a) Distribution of the glaciation temperature considering two regimes defined by the cloud area: $A < 129$ pixels and $A > 467$ pixels. (b) Same as (a) but considering two regimes defined by the large scale vertical velocity ω_{500}: ω_{500}, < −0.0033 Pa/s and ω_{500}, >0.0385 Pa/s. (c) Same as (a) but considering two regimes defined by the cloud optical thickness (τ): τ <11 and τ ≥100. (d) Same as (a) but considering two regimes defined by the convective available potential energy (C3APE): *CAPE*, <11.0 J/kg and *CAPE*, >476.5 J/kg. (e) Same as (a) but considering two regimes defined by the ice crystal effective radius r_e^{Ice}: $r_e^{Ice}(t+1\ \Delta t)$, <11.5 μm and $r_e^{Ice}(t+1\ \Delta t)$, >22.1 μm. (f) Same as (a) but considering two regimes defined by the cloud droplet effective radius r_e^{Liq}: $r_e^{Liq}(t-1\ \Delta t)$, <11 μm and $r_e^{Liq}(t-1\ \Delta t)$, >20 μm. The dashed lines represent the median of each distribution and the dashes line in pastel colors represent the 25th and 75th percentiles. The distributions are normalized; that is, each distribution represents the value of the probability density function and the integral over the range is one.

lower and upper quartiles of T_g in degree celsius between the parenthesis. It should be noted that, due to the coarse resolution of SEVIRI, T_g is probably underestimated. We retrieve T_g considering different regimes based on the maximum cloud area (A^{max}), the maximum τ (τ_{max}), r_e^{Liq} two Δt before the phase transition ($r_e^{Liq}(t_0 - 2\Delta t)$), r_e^{Ice} two Δt after the phase transition ($r_e^{Ice}(t_0 + 2\Delta$ t)), CAPE, and ω_{500} both considered at the closest time to t_0. We define two regimes for each parameter; the first regime considers values less than the first quartile and the second regime considers values greater than the third quartile.

Figure 5 shows the distributions of T_g, and Table 1 shows the median, lower, and upper quartiles of T_g for the different regimes mentioned above. The medians T_g for the two regimes of A^{max}, $\omega_{500}(t_0)$, and τ^{max} are similar. Indeed, A^{max} less than 129 pixels are associated with a median T_g of −22.2°C and A^{max} greater than 467 pixels are associated with a median T_g of −23.7°C. Clouds with a $\omega_{500}(t_0)$ less than −0.33 hPa/s are associated with a median T_g of −21.7°C and clouds with $\omega_{500}(t_0)$ greater than 3.85 hPa/s are associated with a median T_g of −20.7°C. Clouds with τ^{max} less than 11 are associated with a median T_g of −25.7°C and clouds with τ^{max} greater than 100 are associated with a median T_g of −22.2°C. For the three parameters discussed above, the p values from the Kolmogorov-Smirnov test (Massey, 1951) show that the distributions between the two regimes are similar ($p > 0.01$).

Figures 5d, 5e, and 5f show the T_g distribution for the two regimes of CAPE(t_0), $r_e^{Ice}(t_0+2\Delta t)$, and $r_e^{Liq}(t_0-2\Delta t)$. We can notice that the lower and upper quartiles of $r_e^{Ice}(t_0 + 2\Delta$ t) and $r_e^{Liq}(t_0 - 2\Delta t)$ are similar, which can be surprising: We expect $r_e^{Ice}(t_0 + 2\Delta t)$ to be larger than $r_e^{Liq}(t_0 - 2\Delta$ t), but the similar values are an artifact

Table 1
Median Glaciation Temperature for the Regimes Defined by the 25th and 75th Percentiles of Each Parameter

Parameter	T_g when parameter <1st quartile	T_g when parameter >3rd quartile	ΔT_g (°C)	p
A^{max}	−22.2 (−10.8; −30.0)	−23.7 (−12.6; −34.2)	−2	0.676
$r_e^{Liq}(t_0 - 2\ \Delta t)$	−24.7 (−16.7; −35.7)	−13.7 (−7.5; −28.5)	11	**0.000**
$r_e^{Ice}(t_0 + 2\ \Delta t)$	−33.2 (−20.9; −39.9)	−18.2 (−8.15; −26.7)	15	**0.000**
CAPE	−23.9 (−16.0; −36.4)	−17.2 (−10.4; −29.2)	6	**0.002**
ω_{500}	−21.7 (−12.2; −34.2)	−20.7 (−11.2; −28.7)	1	0.208
τ^{max}	−25.7 (−14.4; −38.7)	−22.2 (−13.0; −33.2)	4	0.011

Note. The numbers in parenthesis are the first and third quartile of the glaciation temperature of each regimes. ΔT_g is the difference in glaciation temperature between the two regimes of parameters. The p value is retrieved from the Kolmogorov-Smirnov test to determine if the two distributions are similar. p values less than 0.01 are highlighted in bold and indicate different T_g distributions for the different regimes.

around the phase transition already described by Coopman et al. (2019) and explained earlier. Clouds with CAPE(t_0) less than 11 J/kg are associated with a median T_g of −23.9°C and clouds with CAPE(t_0) greater than 476.5 J/kg are associated with a median T_g of −17.2°C. The CAPE value might seem low for summer-time convection CAPE, but due to the temporal and spatial resolution of ERA-Interim, our CAPE values correspond to the environment of clouds rather than the convective and cloudy air parcel. Similarly, clouds with $r_e^{Liq}(t_0 - 2\Delta\ t)$ less than 11 μm are associated with T_g of −24.7°C and clouds with $r_e^{Liq}(t_0 - 2\Delta t)$ greater than 20 μm are associated with T_g of −13.7°C. Finally, clouds with r_e^{Ice} less than 11.5 μm are associated with T_g of −33.2°C and clouds with $r_e^{Ice}(t_0 + 2\Delta\ t)$ greater than 22.1 μm are associated with T_g of −18.2°C. For the three parameters, the p value of the Kolmogorov-Smirnov test is less than 0.01, so we can reject the null hypothesis of equal averages: The two distributions for each regime of the parameters are different with a confidence greater than 99%.

Table 1 summarizes the variation of T_g for the different regimes, described above. We observe that the larger the r_e, the higher the T_g with a difference of 11°C for $r_e^{Liq}(t_0 - 2\Delta t)$ and 15°C for $r_e^{Ice}(t_0 + 2\Delta t)$. The two regimes of CAPE(t_0) have a difference in T_g of 6°C: High CAPE(t_0) is associated with unstable atmosphere that can enhance the phase transition.

Figure 6 shows the five different parameters as a function of each other, and Table 2 shows the correlation coefficients. We observe a strong correlation of T_g with the CTH, with a correlation coefficient (r) equal to −0.86. As mentioned above, in CLAAS-2, CTT is directly retrieved from CTH and a temperature profile from ERA-interim. We observe that r_e^{Ice} is also correlated with T_g with $r = 0.41$ as shown in Table 2: Homogeneous freezing, occurring at −38°C, produces smaller ice crystals than heterogeneous freezing. In the mean time, r_e^{Ice} is also negatively correlated with CTH with $r = -0.35$. It is difficult to disentangle the effect of one parameter on T_g because the different parameters are intercorrelated with each other (Gryspeerdt et al., 2016). In the next section, we describe a method to disentangle the parameters and quantify the correlation between them.

Table 2
Linear Correlation Between the Parameters from Figure 6

Parameter	A^{max}	$r_e^{Liq}(t_0 - 2\Delta t)$	$r_e^{Ice}(t_0 + 2\Delta t)$	CTH(t_0)	CAPE(t_0)	$\omega_{500}(t_0)$	T_g
A^{max}	1.00	−0.03	0.01	0.05	0.04	−0.02	0.01
$r_e^{Liq}(t_0 - 2\Delta t)$		1.00	0.11	−0.10	0.27	−0.22	0.25
$r_e^{Ice}(t_0 + 2\Delta t)$			1.00	−0.35	0.01	−0.06	0.41
CTH(t_0)				1.00	0.03	−0.10	−0.87
CAPE(t_0)					1.00	−0.17	0.19
$\omega_{500}(t_0)$						1.00	−0.01
T_g							1.00

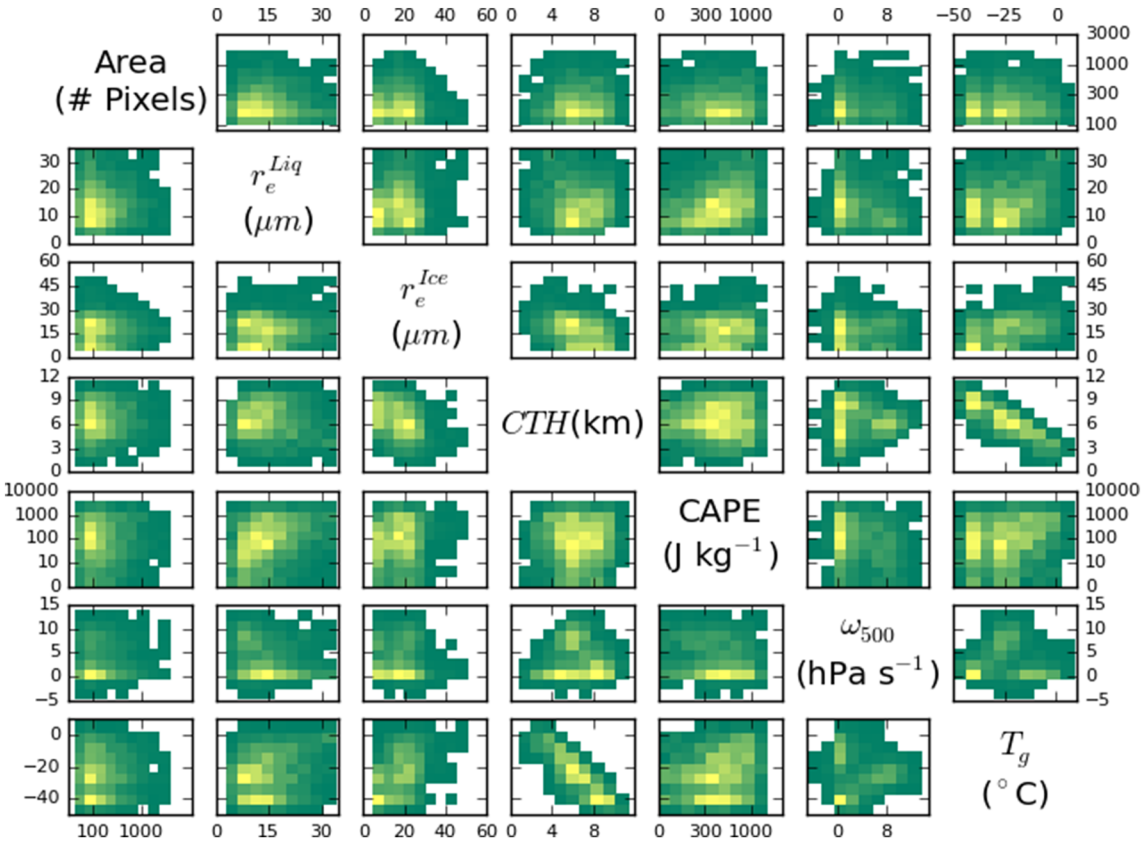

Figure 6. Two-dimensional histogram of the CTH, A, r_e^{Liq}, r_e^{Ice}, CAPE, ω_{500}, and T_g as a function of each other. Yellow colors represent a higher density of point than green colors.

3.3. Principal Component Analysis

As described in section 2.4, we perform the PCA considering six parameters: $\overline{A^{max}}$, $\overline{r_e^{Liq}(t_0 - 2\Delta t)}$, $\overline{r_e^{Ice}(t_0 + 2\Delta t)}$, $\overline{CTH(t_0)}$, $\overline{CAPE(t_0)}$, and $\overline{\omega_{500}(t_0)}$. We have 20 points defined by T_g regimes in the six-dimensional space described by the parameters. Figure 2b shows the number of tracked clouds for each time step, as shown in Figure 2a, for the different regimes of T_g. We observe that the number of tracked clouds at the phase transition is not strictly constant for each regime and range from 32 to 44 because some tracked clouds have the same T_g. For high T_g, the number of clouds in the liquid phase is higher than for low T_g; on the opposite, for low T_g, the number of clouds in the ice phase is higher than for high T_g.

Table 3 shows the eigenvalues associated with the different components from the PCA. We observe that Component 1 has the highest value with an eigenvalue of 3.2 and is therefore the most important component to describe T_g variability—Component 2 is the second most important component with an eigenvalue equal to 1.1. Components 3, 4, 5, and 6 have eigenvalues less than one, which means that their variability is less than the explained variance of the individual initial parameters. According to the Kaiser criterion, we discard them for the study (Costello & Osborne, 2005).

Table 3 shows the decomposition of the Components in the six-dimension space from the parameters. Component 1 is described as (−0.17, 0.44, 0.25, −0.54, 0.40, 0.35) in the base (A^{max}, $r_e^{Liq}(t_0 - 2\Delta t)$, $r_e^{Ice}(t_0 + 2\Delta t)$, $CTH(t_0)$, $CAPE(t_0)$, $\omega_{500}(t_0)$): Most of the variability of Component 1 is described, in order of importance, by $CTH(t_0)$, $r_e^{Ice}(t_0 + 2\Delta t)$, $r_e^{Liq}(t_0 - 2\Delta t)$, $CAPE(t_0)$, $\omega_{500}(t_0)$, and A^{max}. Most of the variability of Component 2 is determined by A^{max} and $CAPE(t_0)$: Component 2 is described as (−0.81, 0.20, −0.25, 0.10, 0.44, 0.12) in the base (A^{max}, $r_e^{Liq}(t_0 - 2\Delta t)$, $r_e^{Ice}(t_0 + 2\Delta t)$, $CTH(t_0)$, $CAPE(t_0)$, $\omega_{500}(t_0)$).

Considering Component 1, we observe that most of the variability comes from CTH. The temperature from CLAAS-2 is retrieved from CTH in the algorithm and with the temperature profile from ERA-Interim. The

Table 3
Eigenvectors Elements of the Parameters from the PCA

Components	$C1$	$C2$	$C3$	$C4$	$C5$	$C6$
Eigenvalue	3.16	1.12	0.84	0.58	0.20	0.09
A^{max}	−0.17	0.81	−0.33	−0.31	−0.31	0.08
$r_e^{Liq}(t_0 - 2\Delta t)$	0.44	0.20	0.40	0.49	−0.57	0.12
$r_e^{Ice}(t_0 + 2\Delta t)$	0.25	−0.25	−0.19	0.46	−0.10	0.67
$CTH(t_0)$	−0.54	0.10	0.15	0.35	0.21	0.73
$CAPE(t_0)$	0.40	0.46	0.44	-0.14	0.64	0.01
$\omega_{500}(t_0)$	0.35	0.12	-0.70	0.54	0.29	0.02

CTT and CTH are correlated from the measurements. We also observe that, on average, large cloud droplets are associated with higher phase transition temperature.

From the PCA, a new space is defined by independent components in which the parameters are described. Here, we only focus on the first two components. In the 2-D space defined by Components 1 and 2, the linearity (v) between parameters is analyzed via the dot product as

$$v = \vec{P}_1 \cdot \vec{P}_2, \tag{6}$$

with $\vec{P}_1$ and $\vec{P}_2$, two parameters described in the space of components both with dimension equal to six, for example, $\overrightarrow{CTH}$ and $\vec{r}_e^{liq}$. If the cosine between two parameters from the 2-D space described by the components is equal to 1 (−1), then the two parameters are collinear (anti-linear). On the opposite, if the cosine is close to 0, then the two parameters are independent from each other. Here, we associate the collinearity to the correlation between two parameters; it is performed as a qualitative rather than quantitative study. Also, it should be noted that the collinearity discussed here is related to the phase transition variation. If the variation of $\vec{P}_1$ impact $\vec{P}_2$, the two parameters are collinear if v is close to 1 or anti-linear if v is close to 0.

Figure 7 and Table 4 show the collinearity of the parameters with each other inspired by Figure 10 from Senf and Deneke (2017). We observe that the highest collinearity is between $\omega_{500}(t_0)$ and $r_e^{Liq}(t_0 - 2\Delta t)$, where the collinearity is 0.97 and for which larger $\omega_{500}(t_0)$ (larger downdraft) is associated with smaller cloud droplets.

4. Discussion

Figures 6 and 7 show results from different methods but with the same data set, and the comparison shows the same variability between the different parameters: For example, smaller CAPE is associated with smaller r_e^{Liq} with both methods. We discuss and hypothesize on some of the correlations that are retrieved by the PCA and shown in Figure 7.

We can observe that large $CTH(t_0)$ are associated with smaller $r_e^{Liq}(t_0 - 2\Delta t)$ with a collinearity of 0.95. We hypothesize that it is easier for small ice crystals to reach higher altitude with the updraft than for large ice crystals more likely to sediment. Also, small crystals are therefore found at colder cloud top, where water vapor is not available to allow ice crystals to grow.

Larger CTH have been observed associated with larger r_e^{Liq} in previous studies (e.g., Rosenfeld & Lensky, 1998; Yuan et al., 2010). The signal observed by the present study (smaller r_e^{Liq} before glaciation correlates

Table 4
Linearity Between the Parameters in the Space Defined by the Components From the PCA

Parameter	A^{max}	$r_e^{Liq}(t_0 - 2\Delta t)$	$r_e^{Ice}(t_0 + 2\Delta t)$	$CTH(t_0)$	$CAPE(t_0)$	$\omega_{500}(t_0)$
A^{max}	1.0	0.26	−0.64	0.39	0.60	0.11
$r_e^{Liq}(t_0 - 2\Delta t)$		1.00	0.60	−0.81	0.91	0.99
$r_e^{Ice}(t_0 + 2\Delta t)$			1.00	−0.96	0.22	0.69
$CTH(t_0)$				1.00	−0.49	−0.87
$CAPE(t_0)$					1.00	0.85
$\omega_{500}(t_0)$						1.00

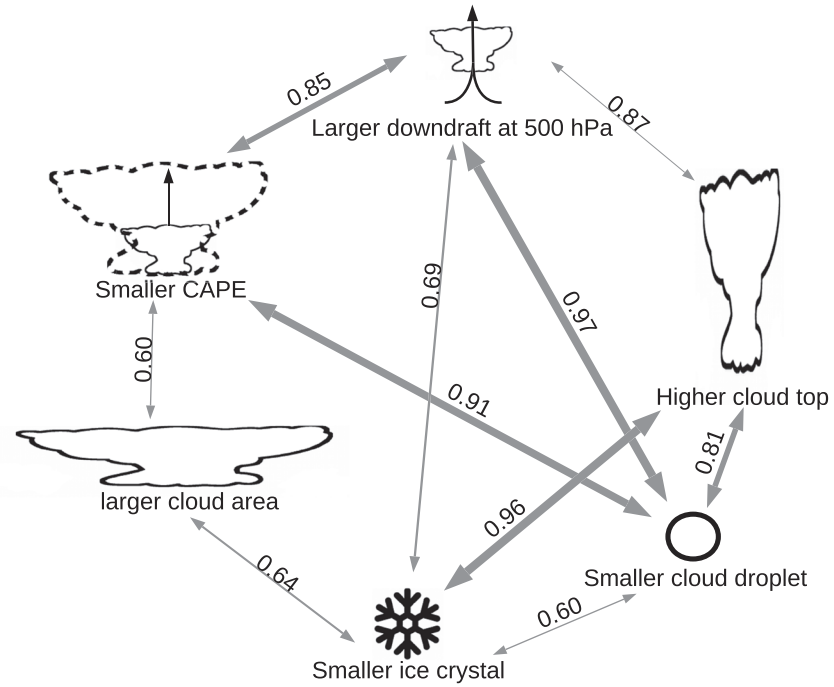

Figure 7. Sketch of connections between the different parameters analyzed with respect to the variation in T_g. The values represent the collinearity between the parameters from the PCA. Only arrows with a dot product between two parameters greater than 0.5 are represented.

with large CTH) can be explained by the presence of overlying clouds as described by Rosenfeld and Lensky (1998), in line with the smaller CAPE and the larger downdraft at 500 hPa. Note that the CTH used in the present study refers to the initiation of the phase transition, so it does not correspond to the CTH considered by Rosenfeld and Lensky (1998) and Yuan et al. (2010).

Our results also indicate that smaller ice crystals are associated with larger cloud area. The anvil extent is driven by the advection of ice crystals from the convective core—source—and the sedimentation—sink. If the ice crystal is small, the sedimentation is reduced and therefore the cloud can extend. An other explanation is that smaller crystals are also associated with larger downdrafts, which would increase the advection and therefore increase the cloud area. These results have an impact on the radiative balance, especially in the tropics where the size of anvil clouds is crucial to determine if clouds have a warming or cooling effect on the surface (Bony et al., 2016).

We speculate that the higher the $\omega_{500}(t_0)$, the larger the $r_e^{Liq}(t_0 - 2\Delta t)$ is because the larger downdraft are associated with less convective region; therefore, the water uptake is less important than for large updraft (Lamb & Verlinde, 2011). The correlation can also be explained by overlying clouds, which might bias our study.

We observed in sections 3.2 and 3.3 that larger cloud droplets are associated with higher T_g. This result has been first observed by Rosenfeld and Lensky (1998) and later by Rangno and Hobbs (2001), Rosenfeld et al. (2011), Coopman et al. (2018), and Coopman et al. (2020) using satellite observations over different regions and speculated that smaller cloud droplets do not support secondary ice process. Therefore, large cloud droplets are more likely to increase the concentration of ice and facilitate the phase transition and the development of the ice phase (Field et al., 2016).

Few studies based on satellite observations have retrieved thermodynamic cloud phase transition temperatures. Rosenfeld and Lensky (1998) developed a method based on the vertical profile of r_e to estimate T_g. Rosenfeld et al. (2011) used this method to retrieve T_g of convective clouds as a function of different cloud droplet size and aerosol type regimes. They retrieved that marine clouds glaciate at −16°C, polluted and/or dusty continental clouds glaciate at temperature ranging from −22°C to −25°C, and clouds associated with smoke from forest fire glaciates at −35°C. They also found a positive correlation between T_g and r_e^{Liq} and

that clouds glaciate at temperatures between −10°C and −38°C for r_e^{Liq} smaller than 12 μm whereas clouds glaciate at temperatures greater than −20°C. We observe that our values of T_g corresponds to these ranges: Europe is impacted by several aerosol types (Querol et al., 2009; Ma & Yu, 2014), which can explain a large variability of T_g.

Coopman et al. (2018) statistically inferred T_g from satellite measurements in the Arctic. They considered that T_g corresponds to the temperature for which 50% of the pixels are in the ice phase for arctic clouds. They found that T_g is on average equal to −17°C. They also considered different regimes of pollution and cloud droplet size: Pollution can increase the glaciation temperature up to 4°C, and they found a positive correlation between T_g and r_e, which is in line with our results, although they apply to a different region and cloud type. Coopman et al. (2020) used the same method to retrieved T_g at different latitudes, microphysical, and meteorological regimes, and they retrieved values between −30°C and −15°C.

Carro-Calvo et al. (2016) retrieved cloud glaciation temperature for different latitudes and altitudes using, respectively, Pathfinder Atmosphere-Extended (PATMOS-x) on Advanced Very High Resolution Radiometer (Heidinger et al., 2014). Carro-Calvo et al. (2016) considered T_g as the temperature where 50% of the pixels are in the ice and liquid phase. They found T_g between −15°C and −38°C, which is in agreement with values retrieved in Table 1. It is not straightforward to compare passive satellite measurements with models: Hoose et al. (2018) showed that some processes such as rime splittering at −10°C are not detectable by passive satellites due to spatial resolution coarser than 1 km. Also, the cloud top phase transition temperature is more likely to be shifted to higher temperatures than in cloud due to a stronger Wegner-Bergeron-Findeisen process at cloud top (Hoose et al., 2018; Korolev et al., 2017). Therefore, when comparing cloud top information from passive satellite with vertical distribution from active satellite, the temperature transition is more likely to be higher for passive satellites.

Senf and Deneke (2017) developed a cloud tracking algorithm for convective clouds over Europe based on the maximum cooling at cloud top. Their study analyzes the correlation between the anvil size, the CTP, the ice crystal size, precipitation, and the area expansion. The first three parameters are in common with our study, and we can compare their results with ours. Senf and Deneke (2017) found that smaller ice crystals are associated with larger cloud area and higher cloud top, in line with our results. Nevertheless, they found a strong correlation between the area of cloud and CTH that we do not observe in our data set. We explain this difference by the fact that they do not consider the parameters at a fixed time but rather when the correlation is maximal. The correlation is the highest 31 min after the maximum cooling at cloud top: Before or after this reference time, the correlation may not be as significant. With our data set, we cannot consider many different time steps, as most of our clouds only have two time steps in the ice phase.

Senf and Deneke (2017) also included precipitation with the cloud properties retrieved from space-based measurements. They showed that more precipitation was associated with larger anvils and smaller ice crystals. Therefore, the higher precipitation rate would be associated with a lower T_g in our data set. This results can be explained as it is related also with a higher cloud top and larger cloud area, more likely for strong convective system.

5. Conclusion

Our analysis is based on the temporal evolution of cloud microphysical properties of isolated convective clouds during summer over Europe from 2004 and 2015. We were able to track 796 clouds and to follow the temporal evolution of their microphysical properties based on the space-based instrument SEVIRI. For example, following the mean temporal evolution of CTT, we observe a decrease with time, faster at the phase transition: CTT goes on average from −13°C one time step before the phase transition to −31°C one time step after the phase transition. We observed that T_g depends on r_e^{Liq} in line with previous studies (e.g., Rosenfeld & Lensky, 1998; Rosenfeld et al., 2011): An increase in T_g by 11.1°C is retrieved when the cloud droplet size goes from lower than 11 μm—the lower quartile—to greater than 20 μm—the upper quartile of r_e^{Liq} distribution. Also, T_g decreases by 6°C when CAPE goes from less than 11 to 477 J/kg. Unfortunately, it is difficult to disentangle the effect of the parameters on T_g. We applied a principal component analysis to observe qualitatively the importance of each parameter on T_g, and we quantify the collinearity between the different parameters. We found that the size of ice crystal are strongly related with the size of cloud droplets and CTH. Concerning the phase transition, it is important to take into account the different correlations

before assessing any effect on T_g. This does not only apply to the phase transition analysis but remains accurate for any study with observations (Gryspeerdt et al., 2015).

Passive satellite instruments retrieve cloud properties at cloud top so the phase transition considered here is at cloud top. It would be interesting to couple our data with active satellite sensor to retrieve information on the vertical profile of cloud properties and retrieve more information, such as cloud droplet concentration with the liDAR/raDAR algorithm based on CloudSAT and CALIPSO measurements (Delanoë & Hogan, 2008, 2010). Previous studies tracking cloud properties have included precipitation data from models (Patou et al., 2018) or radar reflectivity (Senf & Deneke, 2017), it would be interesting to investigate the correlation between the phase transition and the precipitation from tracked clouds. A parametrization of T_g from machine learning based on more tracked clouds could improve global models (Andersen et al., 2017). Also, convection remains challenging for weather forecast (Yano et al., 2018); our study could help to improve the prediction in the numerical models for the evolution of convective clouds. Finally, aerosols can act as ice nuclei, but they have not been studied here, only briefly mentioned in the discussion section. it would be interesting to couple our data set with reanalaysis to colocate aerosol information with the tracked clouds to study the aerosol impacts on T_g.

Data Availability Statement

The CLAAS-2 data set can be found online (https://doi.org/10.5676/EUM_SAF_CM/CLAAS/V002).

Acknowledgments
The authors thank two anonymous reviewers for constructive comments on the manuscript. The authors acknowledge support by the state of Baden-Württemberg through bwHPC. We thank ECMWF, the Large-scale dynamics and predictability group (KIT, Karlsruhe) and Michael Sprenger (ETH Zurich) for the support in providing ERA-Interim data. This project has received funding from the European Research Council (ERC) under the European Union's Horizon 2020 research and innovation program (grant agreement 714062).

References

Andersen, H., Cermak, J., Fuchs, J., Knutti, R., & Lohmann, U. (2017). Understanding the drivers of marine liquid-water cloud occurrence and properties with global observations using neural networks. *Atmospheric Chemistry and Physics*, *17*(15), 9535–9546. https://doi.org/10.5194/acp-17-9535-2017

Benas, N., Finkensieper, S., Stengel, M., van Zadelhoff, G.-J., Hanschmann, T., Hollmann, R., & Meirink, J. F. (2017). The MSG-SEVIRI-based cloud property data record CLAAS-2. *Earth System Science Data*, *9*(2), 415–434. https://doi.org/10.5194/essd-9-415-2017

Berrisford, P., Dee, D., Fielding, K., Fuentes, M., Kallberg, P., Kobayashi, S., & Uppala, S. (2011). The ERA-Interim Archive version 2.0. Reading, UK: ECMWF. www.ecmwf.int/publications

Bley, S., Deneke, H., & Senf, F. (2016). Meteosat-based characterization of the spatiotemporal evolution of warm convective cloud fields over central Europe. *Journal of Applied Meteorology and Climatology*, *55*(10), 2181–2195. https://doi.org/10.1175/JAMC-D-15-0335.1

Bony, S., Stevens, B., Coppin, D., Becker, T., Reed, K. A., Voigt, A., & Medeiros, B. (2016). Thermodynamic control of anvil cloud amount. *Proceedings of the National Academy of Sciences*, *113*(32), 8927–8932. https://doi.org/10.1073/pnas.1601472113

Cantrell, W., & Heymsfield, A. (2005). Production of ice in tropospheric clouds: A review. *Bulletin of the American Meteorological Society*, *86*(6), 795–808. https://doi.org/10.1175/BAMS-86-6-795

Carro-Calvo, L., Hoose, C., Stengel, M., & Salcedo-Sanz, S. (2016). Cloud glaciation temperature estimation from passive remote sensing data with evolutionary computing. *Journal of Geophysical Research: Atmospheres*, *121*, 13,591–13,608. https://doi.org/10.1002/2016JD025552

Coopman, Q., Hoose, C., & Stengel, M. (2019). Detection of mixed-phase convective clouds by a binary phase information from the passive geostationary instrument SEVIRI. *Journal of Geophysical Research: Atmospheres*, *124*, 5045–5057. https://doi.org/10.1029/2018JD029772

Coopman, Q., Riedi, J., Finch, D. P., & Garrett, T. J. (2018). Evidence for changes in Arctic cloud phase due to long-range pollution transport. *Geophysical Research Letters*, *45*, 10,709–10,718. https://doi.org/10.1029/2018GL079873

Coopman, Q., Riedi, J., Zeng, S., & Garrett, T. J. (2020). Space based analysis of the cloud thermodynamic phase transition for varying microphysical and meteorological regimes. *Geophysical Research Letters*, *47*, e2020GL087122. https://doi.org/10.1029/2020GL087122

Costello, A. B., & Osborne, J. W. (2005). Best practices in exploratory factor analysis: Four recommendations for getting the most from your analysis. *Practical Assessment, Research & Evaluation*, *10*(7), 1–9.

Dee, D. P., Uppala, S. M., Simmons, A. J, Berrisford, P., Poli, P., Kobayashi, S., et al.(2011). The ERA-Interim reanalysis: Configuration and performance of the data assimilation system. *Quarterly Journal of the Royal Astronomical Society*, *137*(656), 553–597. https://doi.org/10.1002/qj.828

Delanoë, J., & Hogan, R. J. (2008). A variational scheme for retrieving ice cloud properties from combined radar, lidar, and infrared radiometer. *Journal of Geophysical Research*, *113*, D07204. https://doi.org/10.1029/2007JD009000

Delanoë, J., & Hogan, R. J. (2010). Combined CloudSat-CALIPSO-MODIS retrievals of the properties of ice clouds. *Journal of Geophysical Research*, *115*, D00H29. https://doi.org/10.1029/2009JD012346

Derrien, M. (2013). Algorithm Theoretical Basis Document for Cloud Products (CMa-PGE01 v3.2, CT-PGE02 v2.2 & CTTH-PGE03 v2.2) (*3.2.1*). Lannion: EUMETSAT Satellite Application Facility on Nowcasting and Short range Forecasting.

Derrien, M., & Le Gléau, H. (2005). MSG/SEVIRI cloud mask and type from SAFNWC. *International Journal of Remote Sensing*, *26*(21), 4707–4732. https://doi.org/10.1080/01431160500166128

Field, P. R., Lawson, R. P., Brown, P. R. A., Lloyd, G., Westbrook, C., Moisseev, D., et al. (2016). Chapter 7. Secondary ice poduction—Current state of the science and recommendations for the future. *Meteorological Monographs*, *58*, 1–20. https://doi.org/10.1175/AMSMONOGRAPHS-D-16-0014.1

Gryspeerdt, E., Quaas, J., & Bellouin, N. (2016). Constraining the aerosol influence on cloud fraction. *Journal Geophysical Research: Atmospheres*, *121*, 3566–3583. https://doi.org/10.1002/2015JD023744

Gryspeerdt, E., Stier, P., White, B. a., & Kipling, Z. (2015). Wet scavenging limits the detection of aerosol effects on precipitation. *Atmospheric Chemistry and Physics*, *15*(13), 7557–7570. https://doi.org/10.5194/acp-15-7557-2015

Heidinger, A. K., Foster, M. J., Walther, A., & Zhao, X. (2014). NOAA Climate Data Record (CDR) of Cloud Properties from AVHRR Pathfinder Atmospheres - Extended (PATMOS-x), Version 5.3. NOAA National Centers for Environmental Information: NOAA CDR Program.

Heikenfeld, M., Marinescu, P. J., Christensen, M., Watson-Parris, D., Senf, F., van den Heever, S. C., & Stier, P. (2019). Tobac v1.0: towards a flexible framework for tracking and analysis of clouds in diverse datasets. *Geoscientific Model Development Discussions*, *20*(May), 1–31. https://doi.org/10.5194/gmd-2019-105

Hoose, C., Karrer, M., & Barthlott, C. (2018). Cloud top phase distributions of simulated deep convective clouds. *Journal of Geophysical Research: Atmospheres*, *123*, 10,464–10,476. https://doi.org/10.1029/2018JD028381

Jensen, E. J., Lawson, P., Baker, B., Pilson, B., Mo, Q., Heymsfield, A. J., et al. (2009). On the importance of small ice crystals in tropical anvil cirrus. *Atmospheric Chemistry and Physics*, *9*(15), 5519–5537. https://doi.org/10.5194/acp-9-5519-2009

Komurcu, M., Storelvmo, T., Tan, I., Lohmann, U., Yun, Y., Penner, J. E., et al. (2014). Intercomparison of the cloud water phase among global climate models. *Journal of Geophysical Research: Atmospheres*, *119*, 3372–3400. https://doi.org/10.1002/2013JD021119

Korolev, A., McFarquhar, G., Field, P. R., Franklin, C., Lawson, P., Wang, Z., et al. (2017). Mixed-Phase Clouds: Progress and Challenges. *Meteorological Monographs*, *58*, 5.1–5.50. https://doi.org/10.1175/AMSMONOGRAPHS-D-17-0001.1

Lamb, D., & Verlinde, J. (2011). *Physics and chemistry of clouds*. Cambridge: Cambridge University Press.

Lensky, I. M., & Rosenfeld, D. (2006). The time-space exchangeability of satellite retrieved relations between cloud top temperature and particle effective radius. *Atmospheric Chemistry and Physics*, *6*(10), 2887–2894. https://doi.org/10.5194/acp-6-2887-2006

Ma, X., & Yu, F. (2014). Seasonal variability of aerosol vertical profiles over east US and west Europe: GEOS-Chem/APM simulation and comparison with CALIPSO observations. *Atmospheric Research*, *140-141*, 28–37. https://doi.org/10.1016/j.atmosres.2014.01.001

Massey, F. J. (1951). The Kolmogorov-Smirnov test for goodness of fit. *Journal of the American Statistical Association*, *46*(253), 68–78. https://doi.org/10.1080/01621459.1951.10500769

Mathon, V., & Laurent, H. (2001). Life cycle of Sahelian mesoscale convective cloud systems. *Quarterly Journal of the Royal Meteorological Society*, *127*(572), 377–406. https://doi.org/10.1002/qj.49712757208

Matricardi, M., Chevallier, F., Kelly, G., & Thépaut, J.-N. (2004). An improved general fast radiative transfer model for the assimilation of radiance observations. *Quarterly Journal of the Royal Meteorological Society*, *130*(596), 153–173. https://doi.org/10.1256/qj.02.181

Mecikalski, J. R., & Bedka, K. M. (2006). Forecasting convective initiation by monitoring the evolution of moving cumulus in daytime GOES imagery. *Monthly Weather Review*, *134*(1), 49–78. https://doi.org/10.1175/MWR3062.1

Mecikalski, J. R., Jewett, C. P., Apke, J. M., & Carey, L. D. (2016). Analysis of cumulus cloud updrafts as observed with 1-min resolution super rapid scan GOES imagery. *Monthly Weather Review*, *144*(2), 811–830. https://doi.org/10.1175/MWR-D-14-00399.1

Mecikalski, J. R., MacKenzie, W. M., König, M., & Muller, S. (2010). Cloud-top properties of growing cumulus prior to convective initiation as measured by meteosat second generation. Part II: Use of Visible Reflectance. *Journal of Applied Meteorology and Climatology*, *49*(12), 2544–2558. https://doi.org/10.1175/2010JAMC2480.1

Mecikalski, J. R., MacKenzie, W. M., König, M., & Muller, S. (2010). Cloud-Top Properties of Growing Cumulus prior to Convective Initiation as Measured by Meteosat Second Generation. Part I: Infrared Fields. *Journal of Applied Meteorology and Climatology*, *49*(3), 521–534. https://doi.org/10.1175/2009JAMC2344.1

Meirink, J. F., Roebeling, R. A., & Stammes, P. (2013). Inter-calibration of polar imager solar channels using SEVIRI. *Atmospheric Measurement Techniques*, *6*(9), 2495–2508. https://doi.org/10.5194/amt-6-2495-2013

Meirink, J. F., & van Zadelhoff, G. J. (2016). Algorithm Theoretical Basis Document, SEVIRI Cloud Physical Products, CLAAS Edition 2 (*2.2*). Offenbach: EUMETSAT Satellite Application Facility on Climate Monitoring.

Menzel, W. P., Smith, W. L., & Stewart, T. R. (1983). Improved Cloud Motion Wind Vector and Altitude Assignment Using VAS. *Journal of Climate and Applied Meteorology*, *22*(3), 377–384. https://doi.org/10.1175/1520-0450(1983)022<0377:ICMWVA>2.0.CO;2

Nakajima, T., & King, M. D. (1990). Determination of the optical thickness and effective particle radius of clouds from reflected solar radiation measurements. Part I: Theory. *Journal of the Atmospheric Sciences*, *47*(15), 1878–1893. https://doi.org/10.1175/1520-0469(1990)047<1878:DOTOTA>2.0.CO;2

Patou, M., Vidot, J., Riédi, J., Penide, G., & Garrett, T. J. (2018). Prediction of the Onset of Heavy Rain Using SEVIRI Cloud Observations. *Journal of Applied Meteorology and Climatology*, *57*(10), 2343–2361. https://doi.org/10.1175/JAMC-D-17-0352.1

Platnick, S., King, M. D., Meyer, K. G., Wind, G., Amarasinghe, N., Marchant, B., et al. (2014). MODIS Cloud Optical Properties: User Guide for the Collection 6 Level-2 MOD06/MYD06 Product and Associated Level-3 Datasets. Greenbelt: NASA.

Querol, X., Alastuey, A., Pey, J., Cusack, M., Pérez, N., Mihalopoulos, N., et al. (2009). Variability in regional background aerosols within the Mediterranean. *Atmospheric Chemistry and Physics*, *9*(14), 4575–4591. https://doi.org/10.5194/acp-9-4575-2009

Rangno, A. L., & Hobbs, P. V. (2001). Ice particles in stratiform clouds in the Arctic and possible mechanisms for the production of high ice concentrations. *Journal Geophysical Research*, *106*(D14), 15,065–15,075. https://doi.org/10.1029/2000JD900286

Roberts, R. D., & Rutledge, S. (2003). Nowcasting Storm Initiation and Growth Using GOES-8 and WSR-88D Data. *Weather and Forecasting*, *18*(4), 562–584. https://doi.org/10.1175/1520-0434(2003)018<0562:NSIAGU>2.0.CO;2

Roebeling, R. A., Feijt, A. J., & Stammes, P. (2006). Cloud property retrievals for climate monitoring: Implications of differences between Spinning Enhanced Visible and Infrared Imager (SEVIRI) on METEOSAT-8 and Advanced Very High Resolution Radiometer (AVHRR) on NOAA-17. *Journal of Geophysical Research*, *111*, D20210. https://doi.org/10.1029/2005JD006990

Rosenfeld, D., & Lensky, I. M. (1998). Satellite-Based Insights into Precipitation Formation Processes in Continental and Maritime Convective Clouds. *Bulletin of the American Meteorological Society*, *79*(11), 2457–2476. https://doi.org/10.1175/1520-0477(1998)079<2457:SBIIPF>2.0.CO;2

Rosenfeld, D., Yu, X., Liu, G., Xu, X., Zhu, Y., Yue, Z., et al. (2011). Glaciation temperatures of convective clouds ingesting desert dust, air pollution and smoke from forest fires. *Geophysical Research Letters*, *38*, L21804. https://doi.org/10.1029/2011GL049423

Saunders, R., Matricardi, M., & Brunel, P. (1999). An improved fast radiative transfer model for assimilation of satellite radiance observations. *Quarterly Journal of the Royal Meteorological Society*, *125*(556), 1407–1425. https://doi.org/10.1002/qj.1999.49712555615

Schmetz, J., Holmlund, K., Hoffman, J., Strauss, B., Mason, B., Gaertner, V., et al. (1993). Operational Cloud-Motion Winds from Meteosat Infrared Images. *Journal of Applied Meteorology*, *32*(7), 1206–1225. https://doi.org/10.1175/1520-0450(1993)032<1206:OCMWFM>2.0.CO;2

Schröder, M., König, M., & Schmetz, J. (2009). Deep convection observed by the Spinning Enhanced Visible and Infrared Imager on board Meteosat 8: Spatial distribution and temporal evolution over Africa in summer and winter 2006. *Journal of Geophysical Research*, *114*, D05109. https://doi.org/10.1029/2008JD010653

Senf, F., & Deneke, H. (2017). Satellite-Based Characterization of Convective Growth and Glaciation and Its Relationship to Precipitation Formation over Central Europe. *Journal of Applied Meteorology and Climatology*, *56*(7), 1827–1845. https://doi.org/10.1175/JAMC-D-16-0293.1

Senf, F., Dietzsch, F., Hünerbein, A., & Deneke, H. (2015). Characterization of Initiation and Growth of Selected Severe Convective Storms over Central Europe with MSG-SEVIRI. *Journal of Applied Meteorology and Climatology*, *54*(1), 207–224. https://doi.org/10.1175/JAMC-D-14-0144.1

Stammes, P. (2001). Spectral radiance modelling in the UV-Visible range. In W. L. Smith, & Y. M. Timofeye (Eds.), *Irs 2000: Current problems in atmospheric radiation* (pp. 385–388). Hampton, VA: A. Deepak Publ.

Stengel, M. S., Kniffka, A. K., Meirink, J. F. M., Lockhoff, M. L., Tan, J. T., & Hollmann, R. H. (2014). CLAAS: The CM SAF cloud property data set using SEVIRI. *Atmospheric Chemistry and Physics*, *14*(8), 4297–4311. https://doi.org/10.5194/acp-14-4297-2014

Velicer, W. F. (1976). Determining the number of components from the matrix of partial correlations. *Psychometrika*, *41*(3), 321–327.

Walker, J. R., MacKenzie, W. M., Mecikalski, J. R., & Jewett, C. P. (2012). An Enhanced Geostationary Satellite-Based Convective Initiation Algorithm for 0-2-h Nowcasting with Object Tracking. *Journal of Applied Meteorology and Climatology*, *51*(11), 1931–1949. https://doi.org/10.1175/JAMC-D-11-0246.1

Yano, J.-I., Ziemiański, M. Z., Cullen, M., Termonia, P., Onvlee, J., Bengtsson, L., et al. (2018). Scientific Challenges of Convective-Scale Numerical Weather Prediction. *Bulletin of the American Meteorological Society*, *99*(4), 699–710. https://doi.org/10.1175/BAMS-D-17-0125.1

Yuan, T., Martins, J. V., Li, Z., & Remer, L. A. (2010). Estimating glaciation temperature of deep convective clouds with remote sensing data. *Geophysical Research Letters*, *37*, L08808. https://doi.org/10.1029/2010GL042753

Zinner, T., Mannstein, H., & Tafferner, A. (2008). Cb-TRAM: Tracking and monitoring severe convection from onset over rapid development to mature phase using multi-channel Meteosat-8 SEVIRI data. *Meteorology and Atmospheric Physics*, *101*(3-4), 191–210. https://doi.org/10.1007/s00703-008-0290-y